ORIGIN AND EVOLUTION OF CORONAL STREAMER STRUCTURE DURING THE 1996 MINIMUM ACTIVITY PHASE

Y.-M. WANG, N. R. SHEELEY, JR., R. A. HOWARD, J. R. KRAEMER,[1] N. B. RICH,[2] M. D. ANDREWS,[3]
G. E. BRUECKNER, K. P. DERE, M. J. KOOMEN,[4] C. M. KORENDYKE, D. J. MICHELS, J. D. MOSES,
S. E. PASWATERS,[2] D. G. SOCKER, AND D. WANG[2]

E. O. Hulburt Center for Space Research, Naval Research Laboratory, Washington DC 20375-5352

P. L. LAMY, A. LLEBARIA, AND D. VIBERT

Laboratoire d'Astronomie Spatiale, F-13376 Marseille Cedex 12, France

R. SCHWENN

Max-Planck-Institut für Aeronomie, D-37189 Katlenburg-Lindau, Germany

AND

G. M. SIMNETT

Department of Physics and Space Research, University of Birmingham, Birmingham B15 2TT, England, UK

ABSTRACT

We employ coronal extrapolations of solar magnetograph data to interpret observations of the white-light streamer structure made with the LASCO coronagraph in 1996. The topological appearance of the streamer belt during the present minimum activity phase is well described by a model in which the Thomson-scattering electrons are concentrated around a single, warped current sheet encircling the Sun. Projection effects give rise to bright, jet-like structures or spikes whenever the current sheet is viewed edge-on; multiple spikes are seen if the current sheet is sufficiently wavy. The extreme narrowness of these features in polarized images indicates that the scattering layer is at most a few degrees wide. We model the evolution of the streamer belt from 1996 April to 1996 September and show that the effect of photospheric activity on the streamer belt topology depends not just on the strength of the erupted magnetic flux, but also on its longitudinal phase relative to the background field. Using flux transport simulations, we also demonstrate how the streamer belt would evolve during a prolonged absence of activity.

Subject headings: Sun: activity — Sun: corona — Sun: magnetic fields

1. INTRODUCTION

The physical characteristics of the solar corona are generally thought to be controlled by the Sun's magnetic field. Changes in the magnetic field configuration, caused either by the emergence of new flux or by transport processes at the solar surface, should thus be reflected in the observed evolution of coronal structures. The relation between the corona and the magnetic field is most easily studied during times of low activity, when the sources of emerging flux can be identified more or less unambiguously.

The Large Angle Spectroscopic Coronagraph (LASCO) experiment on board the *Solar and Heliospheric Observatory* (*SOHO*) now provides an unprecedented opportunity to learn about the solar corona under minimum activity conditions. Since the beginning of 1996, the three LASCO coronagraphs have recorded large numbers of high-resolution coronal images over a combined field of view extending from 1.1 to 32 $R_\odot$. In this paper, we analyze and model observations of the outer streamer belt taken in white light between 1996 April and 1996 September. This particular interval was chosen for study because it coincided with the development of an active region complex near the equator. Our main objective will be to determine the effect of the photospheric activity on the coronal streamer structure.

2. OBSERVATIONS

The LASCO instrument comprises three optical systems (designated C1, C2, and C3) with overlapping fields of view (for a detailed description, see Brueckner et al. 1995). This paper employs images taken with the C2 (2–6 $R_\odot$) and C3 (3.7–32 $R_\odot$) coronagraphs. Both C2 and C3 are externally occulted, with the supporting pylon located in the southeast quadrant of the field of view. Each instrument is equipped with a set of polarizers and broadband color filters. The polarizer wheel, which is employed in conjunction with the filter wheel, contains three polarizers whose transmission axes are oriented at $-60°$, $0°$, and $+60°$ to the Sun's east-west axis; there is also a clear glass setting. Each telescope has its own 1024×1024 pixel CCD camera, which records images with a two-pixel spatial resolution of $23''$ (C2) and $112''$ (C3), except near the inner edge of the field of view, where vignetting by the external occulter degrades the resolution.

To illustrate the typical appearance of the white-light streamer structure seen by LASCO during 1996, we display in Figure 1 a sequence of polarized images recorded at approximately 27 day intervals on June 14, July 12, and August 8; the C2 (C3) images are shown in the left-hand (right-hand) column. The polarized intensities $I_{\rm pol}$ ($\equiv pB$) were derived by combining three near-simultaneous images taken with the polarizer wheel set at the $-60°$, $0°$, and $+60°$ positions, using the formula

$$I_{\rm pol} = \tfrac{2}{3}[3(I_{+60} - I_{-60})^2 + (2I_0 - I_{+60} - I_{-60})^2]^{1/2} \quad (1)$$

[1] NRL summer student.
[2] Interferometrics Incorporated.
[3] Hughes STX.
[4] SFA, Incorporated.
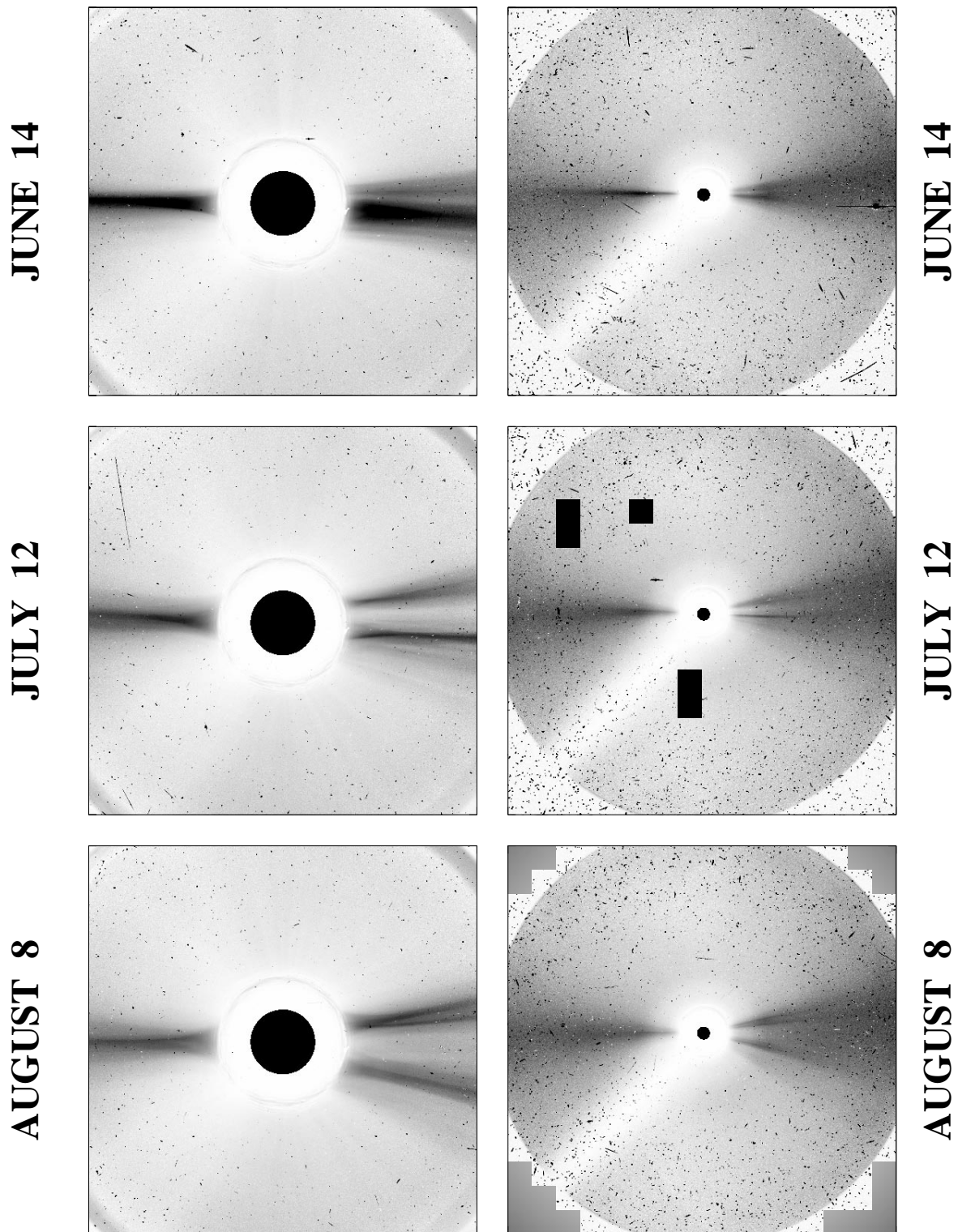
FIG. 1.—Rotation-by-rotation evolution of coronal streamers in polarized light, 1996 June to August. *Left*: LASCO C2 images (2–6 $R_\odot$). *Right*: LASCO C3 images (3.7–32 $R_\odot$). Each image was constructed from three near-simultaneous observations employing the $-60°$, $0°$, and $+60°$ polarizers in combination with the orange filter (band-pass 540–640 nm). The intensities I_{pol} have been scaled by a factor of R^2, where R is the apparent distance from the center of the occulting disk. The regions of highest (lowest) intensity are shown as black (*white*). Black circles indicate the size of the solar disk. (Most of the little specks and streaks in these polarized images are produced by cosmic rays. The small dots with horizontal bars through them are planets, which cause localized saturation or "bleeding" in the CCD; thus Venus appears near the right edge of the June 14 C3 image, while Mercury can be seen to the northeast of the C3 occulting disk on July 12.)

(see Billings 1966). In the case of the C3 observations, the intensities through the polarizers were corrected for differences in their transmission coefficients, as well as for exposure time and offset bias.

With the removal of the unpolarized component (contributed mainly by the dust-scattered F corona), the polarized images of Figure 1 reveal the narrowness of the brightest streamer structures, with characteristic widths of
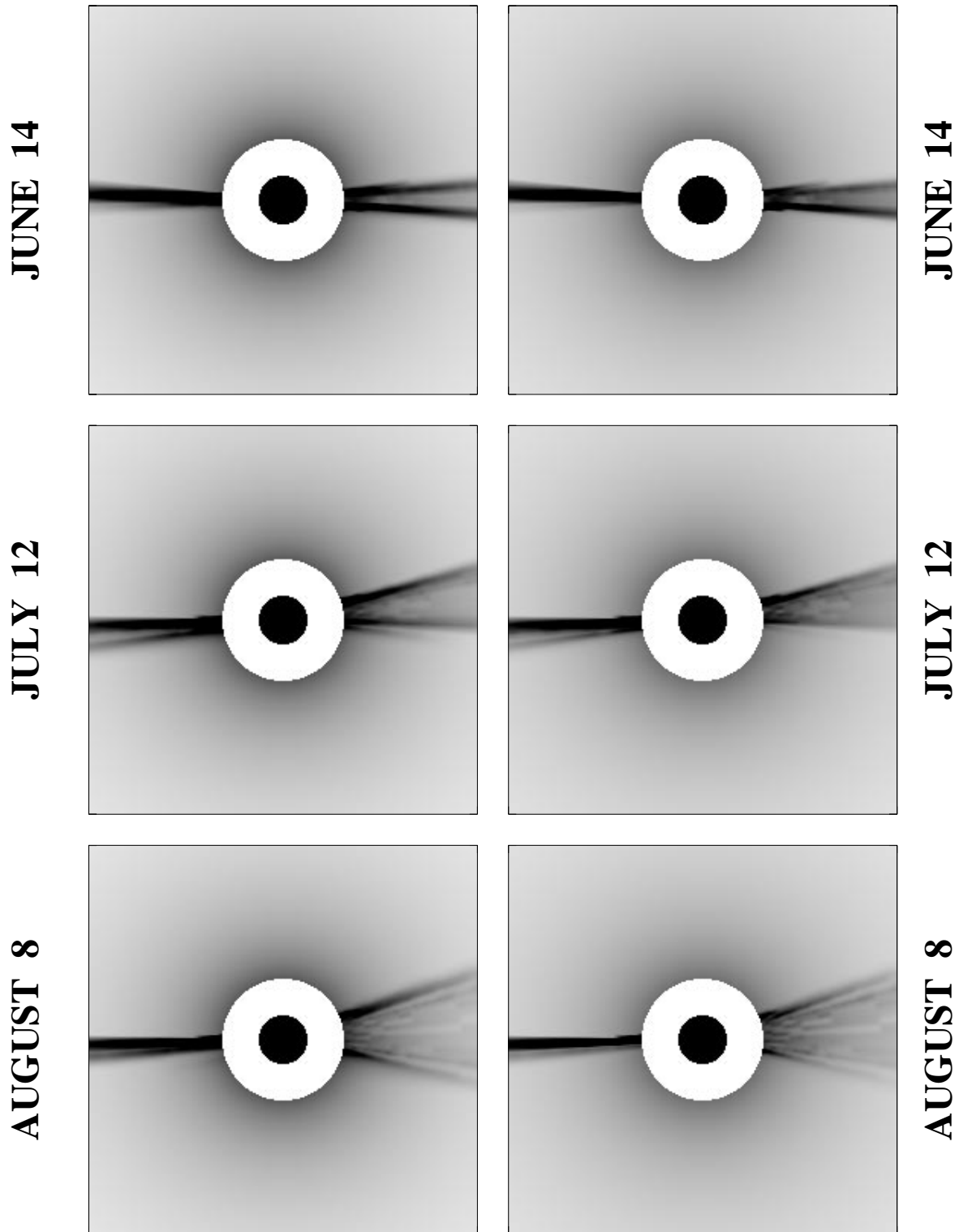
FIG. 2.—Simulated coronal streamers, 2.5–8 $R_\odot$, 1996 June to August (compare the LASCO observations of Fig. 1). The scattering electrons are assumed to be concentrated in a $2\overset{\circ}{.}5$ wide band centered around the current sheet, whose location was determined by an outward extrapolation of the WSO photospheric field for CR 1910, 1911, and 1912, respectively. *Left*: total intensity $K_{\rm tot} = K_{\rm tan} + K_{\rm rad}$. *Right*: polarized intensity $K_{\rm pol} = K_{\rm tan} - K_{\rm rad}$. Black circles indicate the size of the solar disk.

$5°$ or less. Each image shows a single, equatorial "jet" at the Sun's east limb and a two-pronged structure at its west limb, which widens from one rotation to the next. Some of the jetlike features appear to consist of even narrower jets; indeed, the general impression is that the whole streamer belt consists of fine spikes. In the following sections, we demonstate how the narrow structures seen in Figure 1 may arise from simple projection effects associated with a single, warped current sheet encircling the Sun. (The close relationship between the coronal streamer belt and the heliospheric current sheet has been recognized since the 1970s: see, e.g., Howard & Koomen 1974; Pneuman, Hansen, & Hansen

1978; Bruno, Burlaga, & Hundhausen 1982.) We also show how the observed widening of the streamer belt was related to photospheric activity.

3. MODELING PROCEDURE

We simulate the relative intensity distribution of the electron-scattered K corona by the following procedure. We suppose that the scattering electrons are concentrated in a 1 pixel (2°.5 to 5°) wide band centered around the current sheet, where the magnetic field in the outer corona changes its direction from outward to inward. Let K_{tan} (K_{rad}) represent the component of the observed radiation with E vector tangential (normal) to the solar surface, so that the total intensity is $K_{\text{tot}} = K_{\text{tan}} + K_{\text{rad}}$ and the polarized intensity is $K_{\text{pol}} = K_{\text{tan}} - K_{\text{rad}}$. Also, let r denote heliocentric distance, λ heliographic latitude, ϕ Carrington longitude (measured in the direction of the Sun's rotation), $n_e(r, \lambda, \phi)$ the electron density, ds a path element along the line of sight, σ_{T} the Thomson scattering cross section, $I_{\odot}$ the intensity of solar radiation at disk center, and $u = 0.6$ a limb darkening coefficient. Then, from Billings (1966),

$$K_{\text{tot}} = \tfrac{1}{2}\pi\sigma_{\text{T}} I_0 \int_{-\infty}^{+\infty} n_e\{2[(1-u)c + ud]$$
$$- \sin^2 \chi[(1-u)a + ub]\}ds \,, \qquad (2)$$

$$K_{\text{pol}} = \tfrac{1}{2}\pi\sigma_{\text{T}} I_0 \int_{-\infty}^{+\infty} n_e \sin^2 \chi[(1-u)a + ub]ds \,, \qquad (3)$$

$$a = \sin^2 \gamma \cos \gamma \,, \qquad (4)$$

$$b = -\frac{1}{8}\left[1 - 3\sin^2\gamma - \frac{\cos^2\gamma}{\sin\gamma}\right.$$
$$\left. \times (1 + 3\sin^2\gamma)\ln\left(\frac{1+\sin\gamma}{\cos\gamma}\right)\right], \qquad (5)$$

$$c = \frac{4}{3} - \cos\gamma - \frac{1}{3}\cos^3\gamma \,, \qquad (6)$$

$$d = \frac{1}{8}\left[5 + \sin^2\gamma - \frac{\cos^2\gamma}{\sin\gamma}\right.$$
$$\left. \times (5 - \sin^2\gamma)\ln\left(\frac{1+\sin\gamma}{\cos\gamma}\right)\right], \qquad (7)$$

where χ is the angle between a radial vector through the scattering point P and the line of sight and γ is the angle between a radius through P and a tangent from P to the solar surface. For simplicity, the electron density in the scattering layer (whose angular position coincides with that of the current sheet) will be assumed to depend only on the radial coordinate and to fall off as $r^{-2.5}$. The calculated streamer patterns were found to be quite insensitive to the radial dependence adopted for n_e.

The location of the current sheet is determined by an outward extrapolation of the observed photospheric field, in the form of a monthly synoptic map obtained electronically from the Wilcox Solar Observatory (WSO). The WSO data were corrected for the saturation of the Fe I 5250 Å line profile by multiplying the measured fields by the latitude-dependent factor $(4.5 - 2.5 \sin^2 \lambda)$ (see Ulrich 1992; Wang & Sheeley 1995). The corona is assumed to be current-free out to a spherical "source surface" $r = R_{\text{ss}} = 2.5 \ R_{\odot}$, where the tangential field components B_λ and B_ϕ are constrained to vanish, thereby simulating the magneto-

hydrodynamic effect of the outflowing solar wind plasma (see, e.g., Schatten, Wilcox, & Ness 1969; Hoeksema 1984). At the inner boundary $r = R_{\odot}$, we require the radial field component B_r to reduce to the observed photospheric flux distribution (Wang & Sheeley 1992). In the outer region $r > R_{\text{ss}}$, we introduce sheet currents by again matching a potential field (but now including an $l = 0$ monopole contribution) to the absolute value of the source surface field, $|B_r(R_{\text{ss}}, \lambda, \phi)|$, and then restoring the original polarity of the field lines, as prescribed by Schatten (1971). (We ignore here the resulting discontinuity in B_λ and B_ϕ at the matching surface $r = R_{\text{ss}}$.) The current sheet(s), where B_r abruptly changes sign, are located by tracing outward from $r = R_{\text{ss}}$ along field lines.

To illustrate the model, we have simulated the streamer structures for 1996 June 14, July 12, and August 8 using the WSO photospheric field data for Carrington rotations (CR) 1910, 1911, and 1912, respectively. The left-hand (right-hand) panels of Figure 2 show the calculated distribution of K_{tot} (K_{pol}) over the heliocentric range $2.5 \ R_{\odot} < r < 8 \ R_{\odot}$. As in the corresponding LASCO images of Figure 1, we see a bright, narrow equatorial streamer at the east limb and a more complex, two-pronged structure at the west limb, the latter widening from one rotation to the next. On the given dates, the current sheet is viewed edge-on at the east limb but roughly face-on at the west limb (central meridian corresponds to Carrington longitude 180° in the current sheet maps shown in Fig. 7 below). The two west-limb "jets" arise from edge-on portions of the current sheet located in front of and behind the plane of the sky. Because K_{tot} includes the contribution of radially polarized photons, which originate out of the sky plane, these spikelike features appear somewhat more prominently in the images of total intensity than in the polarized images.

4. MULTIPOLE ANALYSIS OF THE SOLAR MINIMUM CORONA

In the model described above, the structure of the outer corona and the topology of the heliospheric current sheet are determined by the low-order multipoles of the photospheric magnetic field. We may write the coronal field in the schematic form

$$B_r(r, \lambda, \phi) = \sum_{l=1}^{\infty} \sum_{m=0}^{l} b_{lm}(r, \lambda, \phi) \,, \qquad (8)$$

where the harmonic components b_{lm} are given in terms of the observed photospheric field $B_r(R_{\odot}, \lambda, \phi)$ by the potential-field source-surface solution (see eqs. [3a], [4], and [5] in Wang & Sheeley 1992). As a measure of the strength of each multipole l at a given radius r, we define the root-mean-square (rms) quantity

$$\langle b_l(r) \rangle = \left[\frac{1}{4\pi}\int b_l^2(r, \lambda, \phi)d\Omega\right]^{1/2} \,, \qquad (9)$$

where $b_l = \sum_{m=0}^{l} b_{lm}$ and the integral is performed over all solid angle Ω. Figure 3a shows the time variation of $\langle b_1(R_{\odot})\rangle$, $\langle b_2(R_{\odot})\rangle$, and $\langle b_3(R_{\odot})\rangle$ over the declining phase of sunspot cycle 22. A striking aspect of this plot is the near-equality of the dipole and octupole strengths, $\langle b_1(R_{\odot})\rangle \simeq \langle b_3(R_{\odot})\rangle$, from mid-1993 onward. This property reflects the strong poleward concentration of the photospheric magnetic flux, which, when averaged over longitude, is distributed approximately as $\sin^7 \lambda$ near sunspot
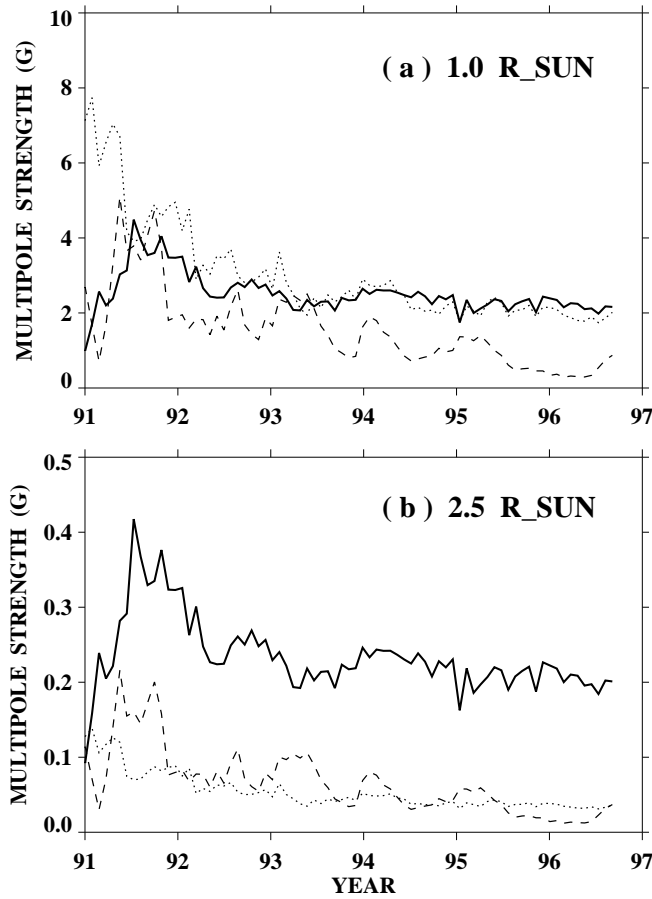
FIG. 3.—Time variation of the Sun's lowest order, rms multipole strengths, evaluated (a) at the photosphere, (b) at $r = 2.5\ R_\odot$. The dipole strength $\langle b_1 \rangle$ is indicated by the solid line, the quadrupole strength $\langle b_2 \rangle$ by the dashed line, and the octupole strength $\langle b_3 \rangle$ by the dotted line. The curves were derived using WSO photospheric field data for CR 1835–1913.
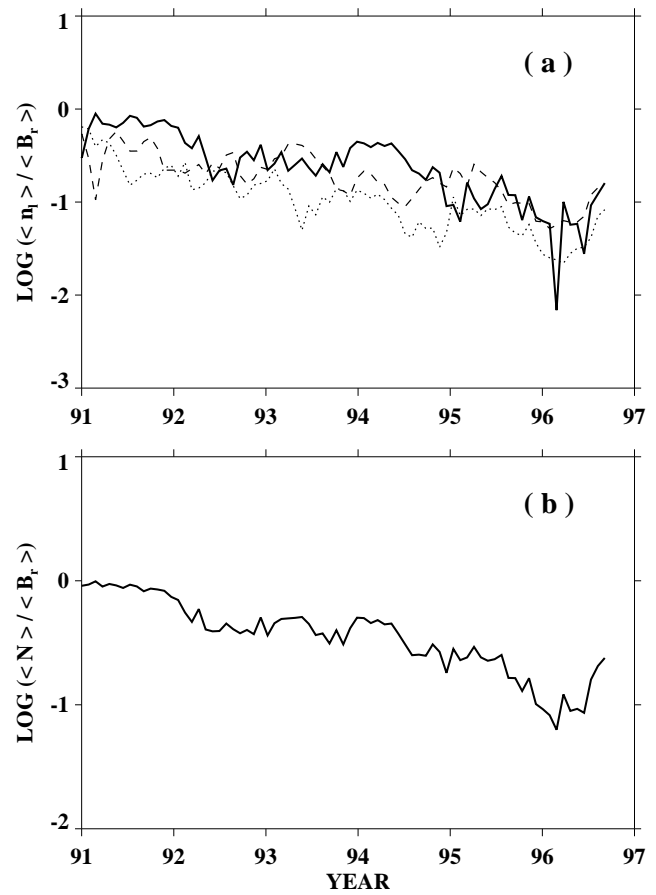
FIG. 4.—Time variation of the nonaxisymmetric $(m \neq 0)$ field components at $r = 2.5\ R_\odot$. (a) Nonaxisymmetric dipole strength $\langle n_1 \rangle$ (solid line), quadrupole strength $\langle n_2 \rangle$ (dashed line), and octupole strength $\langle n_3 \rangle$ (dotted line), all normalized to the total rms field strength $\langle B_r \rangle$ at $r = 2.5$ $R_\odot$. (b) Ratio of the nonaxisymmetric field strength $\langle N \rangle$ (including all multipoles) to the total field strength $\langle B_r \rangle$ at $r = 2.5\ R_\odot$.

minimum (Svalgaard, Duvall, & Scherrer 1978; Wang & Sheeley 1995). The topknot structure of the large-scale photospheric field, which is maintained by a poleward meridional flow (see Wang, Nash, & Sheeley 1989), requires that the axisymmetric $(l = 1, m = 0)$ and $(l = 3, m = 0)$ harmonic components cancel each other at low latitudes.

Because the magnetic multipoles decline with radius as r^{-l-2}, the dipole normally dominates all of the higher-order multipoles by $r \sim 2.5\ R_\odot$ (except around the time of polar field reversal near sunspot maximum). The main contribution to the dipole moment near sunspot minimum comes from its axisymmetric component $(l = 1, m = 0)$, so that the current sheet tends to be flattened toward the heliographic equator. The warping and tilt of the current sheet are determined by the nonaxisymmetric $(m \neq 0)$ components of the low-order magnetic multipoles. To measure the strengths of the latter relative to the total field, we introduce the definitions

$$\langle n_l(r) \rangle = \left[\frac{1}{4\pi} \int (b_l - b_{l0})^2\ d\Omega \right]^{1/2}, \tag{10}$$

$$N(r, \lambda, \phi) = B_r - \frac{1}{2\pi} \int_0^{2\pi} B_r\ d\phi, \tag{11}$$

$$\langle N(r) \rangle = \left[\frac{1}{4\pi} \int N^2\ d\Omega \right]^{1/2}, \tag{12}$$

$$\langle B_r(r) \rangle = \left[\frac{1}{4\pi} \int B_r^2\ d\Omega \right]^{1/2}. \tag{13}$$

Figure 4a displays the temporal behavior of $\langle n_1 \rangle / \langle B_r \rangle$, $\langle n_2 \rangle / \langle B_r \rangle$, and $\langle n_3 \rangle / \langle B_r \rangle$ at $r = 2.5\ R_\odot$ over the declining phase of cycle 22. Similarly, Figure 4b shows the time variation of $\langle N \rangle / \langle B_r \rangle$, representing the relative rms strength of the total nonaxisymmetric field at 2.5 $R_\odot$. The nonaxisymmetric field and its multipole components decline progressively in strength from 1991 onward, reaching a minimum in early 1996. There is then a distinct upturn after the middle of 1996, which is associated with the development of an active region complex near the equator. As will be demonstrated in the next section, the effect of the active region on the large-scale nonaxisymmetric field and on the topology of the streamer belt depends not just on the strength of the erupted flux, but also on its longitudinal phase.

5. EFFECT OF AN ACTIVE REGION ON THE STREAMER BELT TOPOLOGY

Figure 5 shows the observed evolution of the coronal streamer belt over six successive Carrington rotations (CR 1908 through 1913), spanning the period from 1996 April 8 to 1996 September 18. The Carrington format maps have
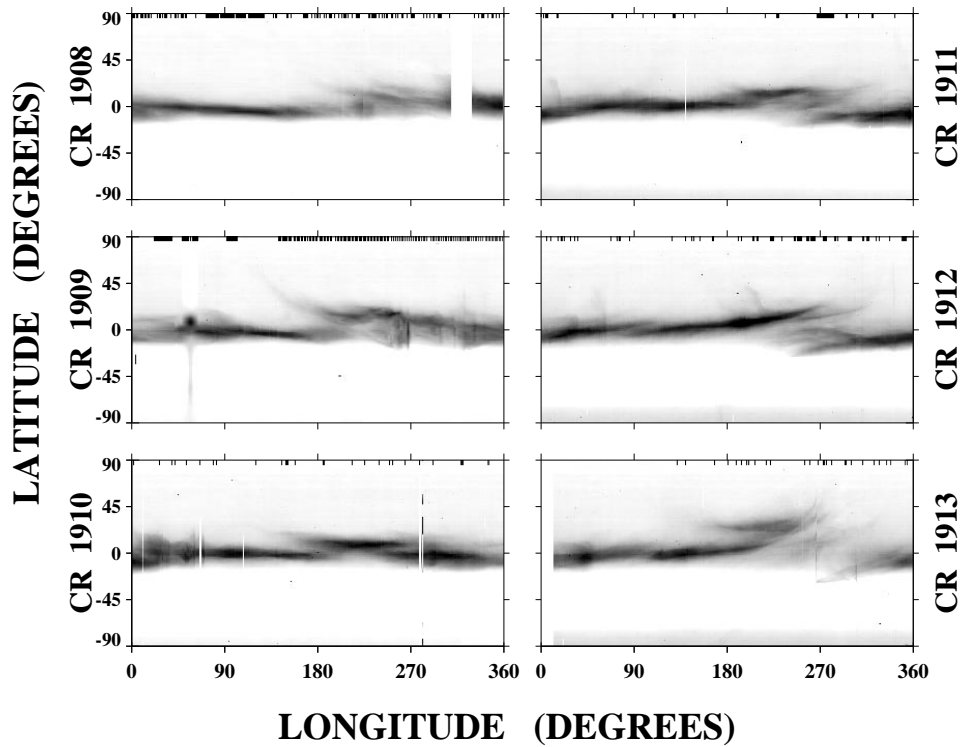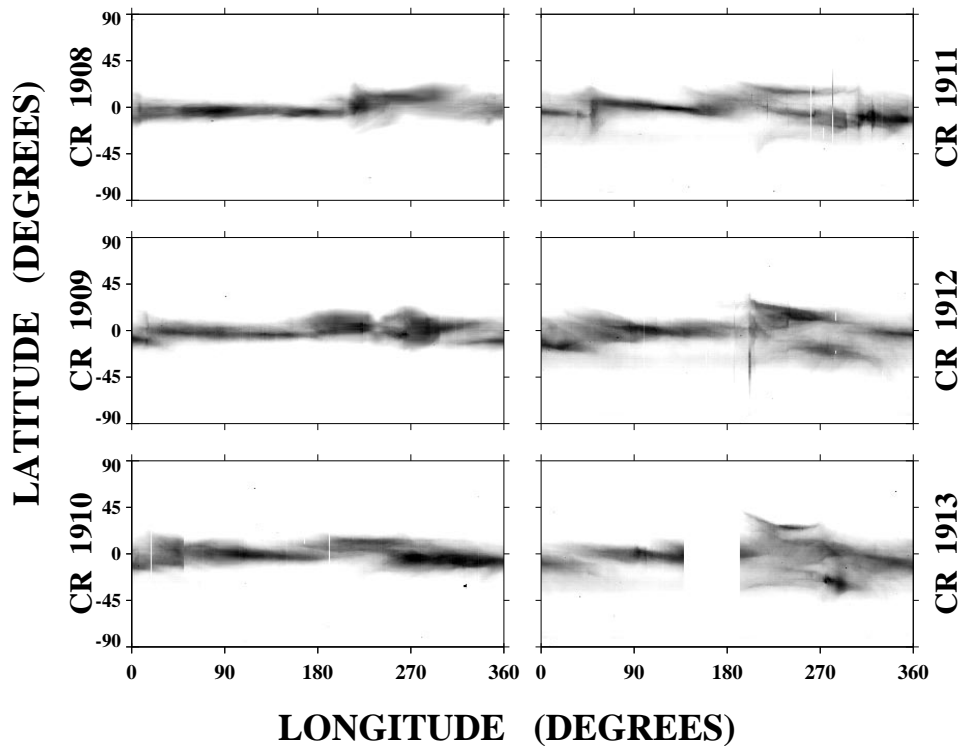
FIG. 5a

FIG. 5b

FIG. 5.—White-light streamer structure at 3.0 $R_\odot$, CR 1908–1913 (1996 April 8 through September 18). (a) East limb observations. (b) West limb observations. To construct these Carrington format maps, slices of east or west limb data were extracted from individual LASCO C2 images (recorded every 1–3 hours) and assembled into time-reversed sequences spanning each Carrington rotation. The brightest (faintest) structures are indicated by black (white). Total intensities are shown, including both polarized and unpolarized components, but with an arbitrary background subtracted. In the east limb maps, the supporting pylon obstructs the field of view in a latitude band between ∼30° south and ∼60° south.

been constructed from many individual C2 images (approximately 340 per rotation), by extracting from each image a slice of east limb (Fig. 5a) or west limb (Fig. 5b) data at a distance of 3 $R_\odot$ from disk center and assembling the slices into a time-reversed sequence. An arbitrary background has been subtracted from the intensities, which include both polarized and unpolarized radiation. (In the east limb maps, the supporting pylon obstructs the field of view between 30° south and 60° south.)

Although we have chosen to display the structures observed at 3 $R_\odot$, the topology of the streamer belt showed little variation between 2.5 and 15 $R_\odot$, except for a very gradual flattening toward the equator and a rapid increase in the contribution of the background F corona. The wispy, arc-like features in Figure 5 which curve away from the equator represent a projection effect, whereby individual structures move to higher (lower) apparent latitudes as they rotate away from (toward) the plane of the sky (see also Figs. 7 and 8 in Wang & Sheeley 1992). (The arcs would be even more prominent in maps of unpolarized or radially polarized intensity, for which a larger proportion of the radiation originates from out of the sky plane.) Because of the tilt of the Sun's rotation axis relative to the sky plane, the arcs exhibit a left-right asymmetry with opposing directions in the northern and southern hemispheres and in the east and west limb maps. Thus, when the north pole is tilted toward the observer (as during CR 1911–1913), the northern-hemisphere (southern-hemisphere) streamers move more rapidly in apparent latitude when they are located behind (in front of) the sky plane, and the ascending and descending portions of the corresponding arcs steepen or flatten accordingly. The converse holds when the south pole is tilted toward the observer (as during CR 1908–1909): the southern-hemisphere (northern-hemisphere) streamers now undergo their most rapid ascent or descent in apparent latitude when located behind (in front of) the sky plane. In addition to this B_0-angle effect, however, Figures 5a and 5b show other significant differences (particularly during CR 1912 and 1913), which suggest intrinsic changes in the streamer structures on time scales less than 14 days.
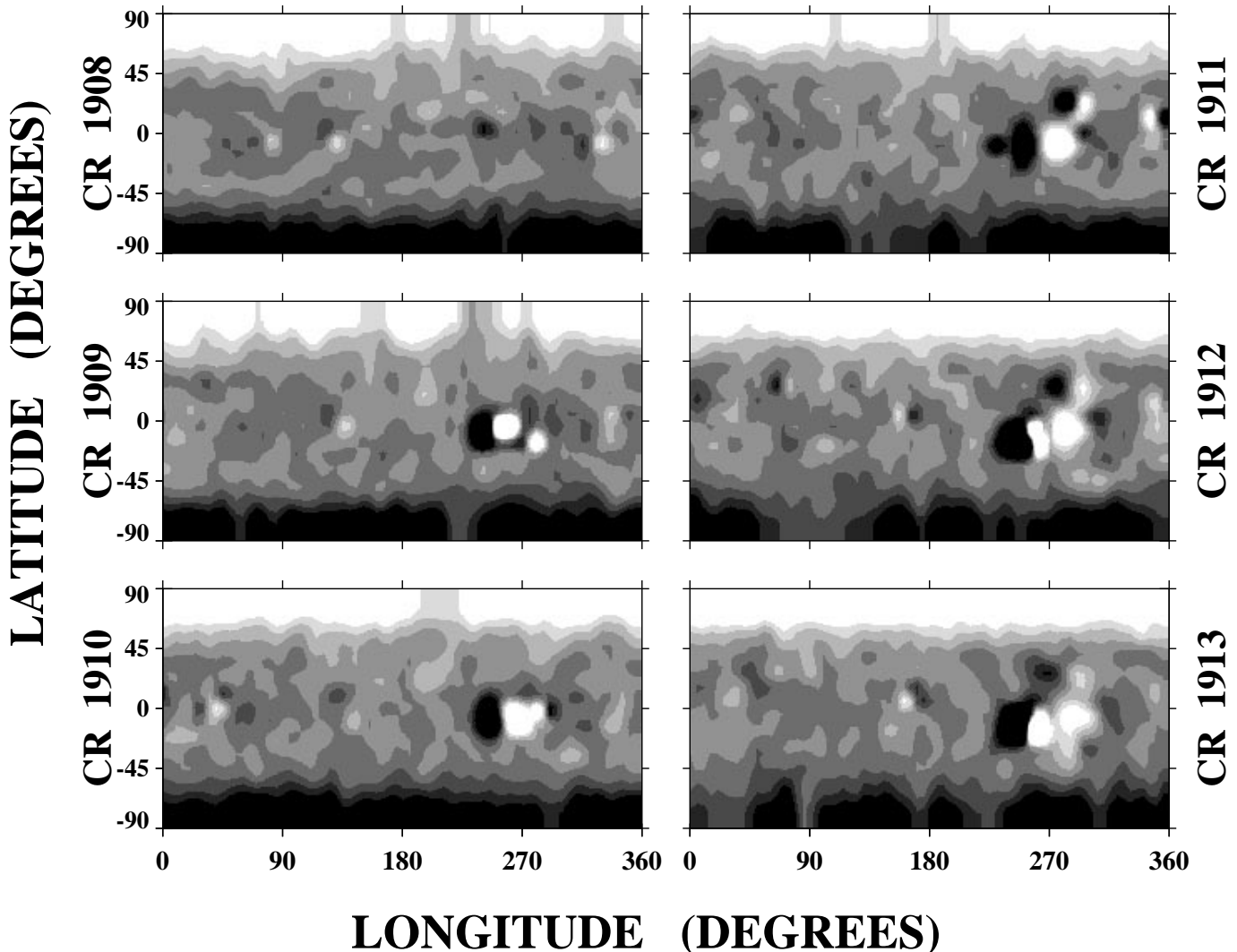

FIG. 6.—Wilcox Solar Observatory (WSO) photospheric field maps, CR 1908–1913. Black denotes strong negative-polarity flux ($B_r \leq -8$ G); white denotes strong positive-polarity flux ($B_r \geq 8$ G), while intermediate shades indicate fields in the range -8 G $< B_r < 8$ G. Because the magnetograph measurements were made around central meridian rather than at the limb, the actual times of observation for the magnetic fields in Fig. 6 lag (precede) those for the east (west) limb streamers in Fig. 5a (Fig. 5b) by approximately 7 days.
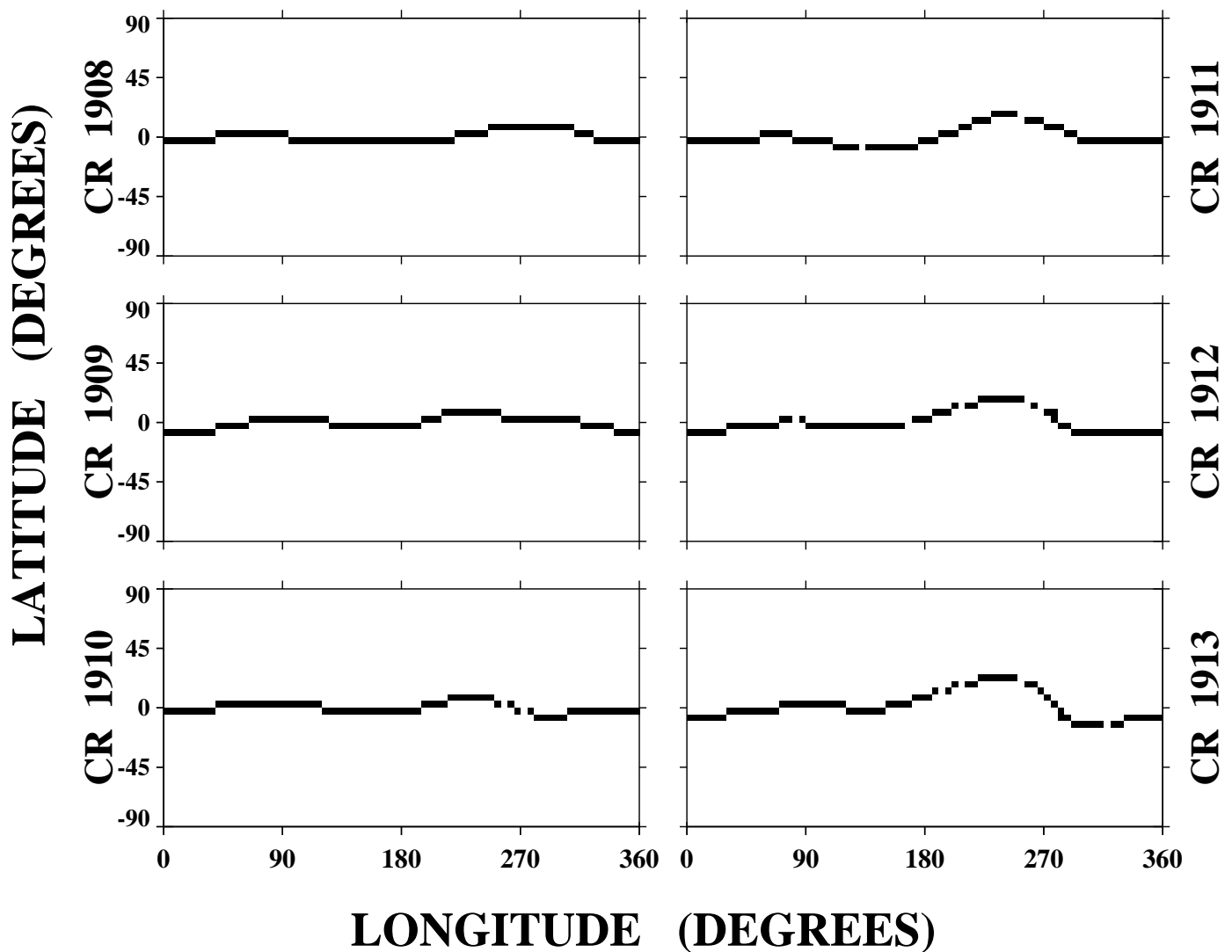
Fig. 7.—Shape of the current sheet at $r = 3.0\ R_\odot$, determined by applying a potential field extrapolation to the WSO photospheric field maps of Fig. 6. The location of the current sheet in latitude and longitude is shown for CR 1908–1913.

It is evident from both the east and west limb maps of Figure 5 that the streamer belt becomes progressively more distorted from CR 1911 (1996 July) onward. For comparison, Figure 6 displays the WSO photospheric field for the same six Carrington rotations. The distortion of the streamer belt is roughly centered above the low-latitude active region complex near longitude 255°. It may be noticed, however, that the initial appearance of a large active region in CR 1909 is not accompanied by any significant change in the streamer topology; it is only two rotations later, when a new active region erupts at approximately the same location as the earlier eruption, that the streamer belt begins to widen appreciably.

To obtain a better understanding of the streamer belt evolution, we now apply the extrapolation model outlined in § 3 to the WSO photospheric field maps. Figures 7 and 8 display, for CR 1908–1913, the computed shape of the current sheet and distribution of $K_{\rm tot}$ at 3.0 $R_\odot$. The model intensities are shown separately for the east (Fig. 8a) and west (Fig. 8b) limbs, the differences in this case arising solely from the B_0-angle projection effect since the same photospheric flux distribution was used to derive the east and west limb maps. The match between the simulated streamer structures and the observed ones (Fig. 5) is generally very good. According to both the model and the observations, the streamer topology remains largely unaffected by the presence of the active region complex until CR 1911. During CR 1912, when substantial intrinsic differences are seen between the east (Fig. 5a) and west limb (Fig. 5b) data, the simulations show better agreement with the east limb map, which employs observations taken 14 days before the corresponding west limb ones. The streamer observed at the southwest limb near longitude 270° may be a new feature since it is not identifiable in the east limb map (even after allowance is made for the asymmetry caused by the B_0-angle projection effect). The sudden brightening and fading of this structure during CR 1913 suggests that it may be rapidly evolving or nonstationary. Time-lapse sequences of C2 and C3 images show a "streamer blowout" mass ejection (as defined by Howard et al. 1985) in the southwest quadrant on September 3 and 4. As indicated by the faint vertical streaks near longitudes 305° and 265° in the east limb map for CR 1913, streamer blowouts also occurred in the southeast quadrant on August 19 and 22, again suggesting rapid changes in the large-scale coronal structure in the vicinity of the active region complex. Some of these events
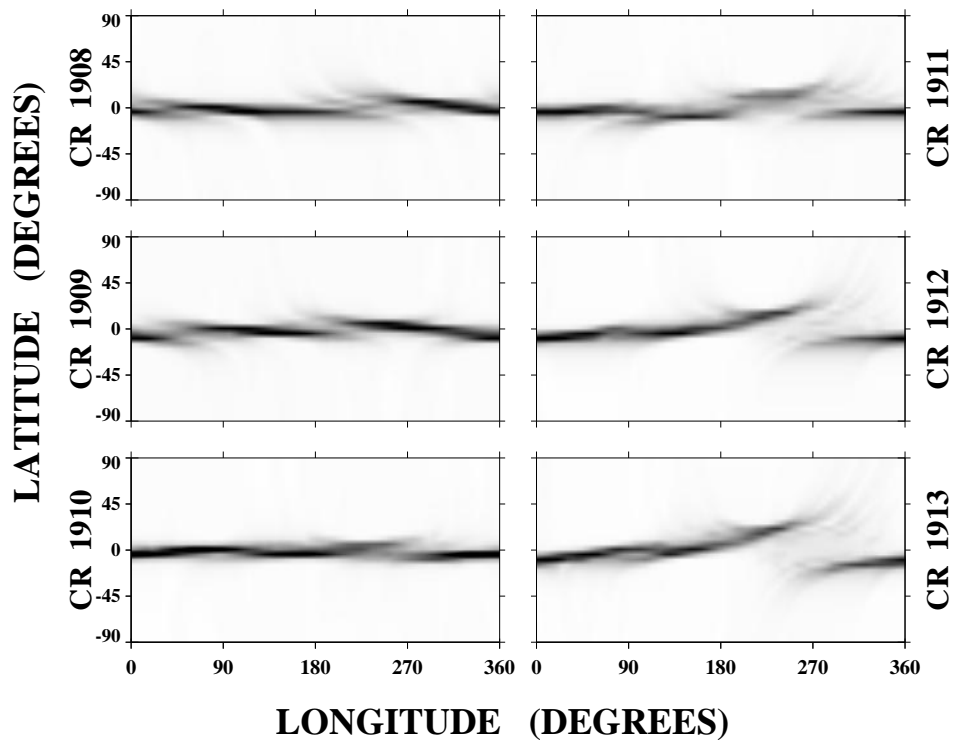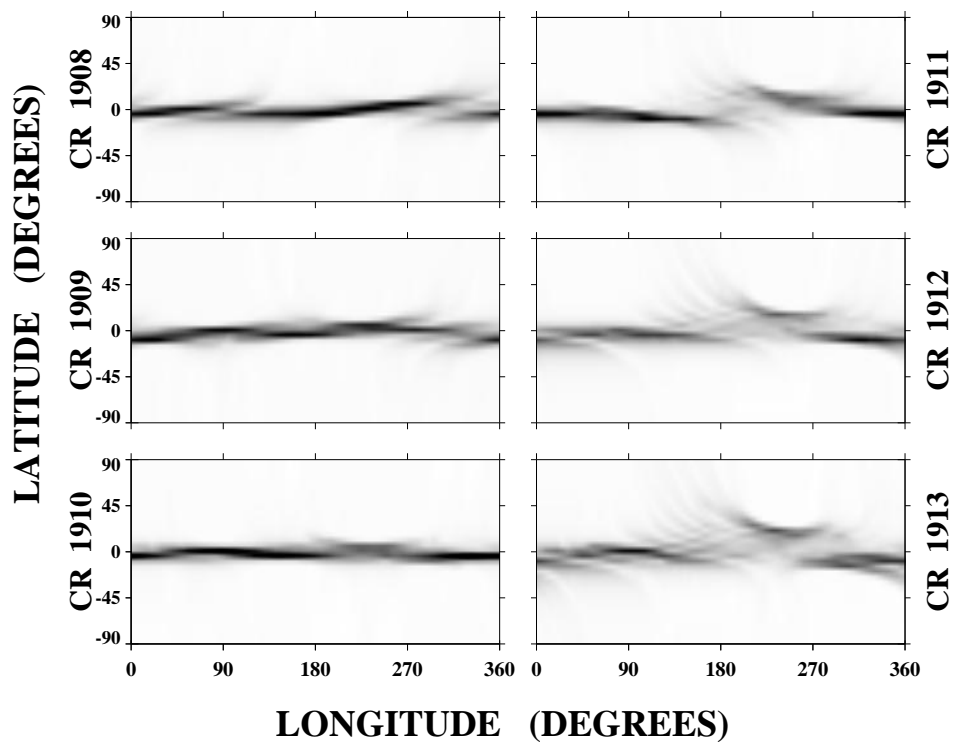
FIG. 8a

FIG. 8b

FIG. 8.—Simulated coronal streamer structures at 3.0 $R_\odot$, CR 1908–1913. (a) East limb maps. (b) West limb maps. The intensities $K_{tot} = K_{tan} + K_{rad}$ were computed by assuming the electrons to be concentrated in a 5° wide layer around the current sheet (see Fig. 7) and integrating the Thomson scattered radiation along the line of sight. The differences between the east and west limb maps are caused by the tilt of the Sun's rotation axis relative to the sky plane, which reaches its maximum value of 7° during CR 1913 (1996 August 22 to September 18), with the north pole pointing toward Earth.

may be related to the development of a trans-equatorial extension of the north polar hole near longitude 290°; this positive-polarity hole (visible, for example, in He I 10830 Å spectroheliograms taken at National Solar Observatory/ Kitt Peak) formed during CR 1912–1913 within the diffuse remnants of the active region that erupted during CR 1909. In the simulations for CR 1913, the new coronal hole is represented by a "finger" of open magnetic field whose southern tip coincides with the slight southward deformation of the current sheet around longitude 300° (see Fig. 7).

As noted in § 4, the distortions of the streamer belt have their origin in the low-order, nonaxisymmetric harmonic components of the photospheric field. In addition to the dipole ($l = 1$), Figure 4a indicates that there is a very substantial quadrupole ($l = 2$) contribution to the non-axisymmetric field during 1996; an accurate representation of the current sheet/streamer topology would in fact require terms up to $l \sim 5$. For simplicity, however, we shall restrict our discussion to the equatorial dipole component ($l = 1$, $|m| = 1$), the evolution of which is shown in Figure 9. We see that the eruption of the active region during CR 1909 shifts the phase of the equatorial dipole eastward by about 70° and slightly decreases its strength (relative to the equatorial dipole field during CR 1908). A corresponding shift occurs in both the observed (Fig. 5) and simulated (Fig. 8) streamer topology. As flux continues to erupt out of phase with the original background field, the net equatorial dipole moment almost vanishes during CR 1910; the small residual warp in the streamer belt and the current sheet stems mainly from the quadrupole and higher-order multipole components. However, new activity in the longitude range 230°–270° regenerates the equatorial dipole field, which grows rapidly in strength and contributes substantially to the widening of the streamer belt from CR 1911 onward.

To illustrate how the longitudinal phase of the erupting flux affects the width of the streamer belt, we have arbitrarily reversed the east-west polarity of the active region complex in CR 1909 (see Fig. 10, left). (In this simulation, the active region was defined to comprise fields $|B_r| \geq 4$ G.) Because the equatorial dipole components of the active region and the background field are now in phase with each other, the derived streamer pattern shows a considerably greater latitudinal excursion than in the original case (Fig. 10, right), where the bipoles erupt out of phase with the background field. (Here and in the remaining simulations, we ignore the B_0-angle effect and assume that the Sun's rotation axis is perpendicular to the line of sight.)

We have thus far assumed that any changes in the streamer topology from one rotation to the next are caused by the emergence of new flux. However, as discussed in Wang & Sheeley (1991), photospheric transport processes such as differential rotation can also alter the relative strengths of the axisymmetric and nonaxisymmetric field components and thus affect the shape of the current sheet and streamer belt. To determine whether the widening of the streamer belt between CR 1911 and CR 1913 can be attributed entirely to such evolutionary effects, we employ the flux transport algorithm of DeVore, Sheeley, & Boris (1984) to advance the observed photospheric field for CR 1911 forward by two rotations, without depositing any new flux (see Fig. 11). The simulation includes the effect of differential rotation, supergranular diffusion, and a poleward meridional flow. The resulting streamer pattern (Fig. 11, left) is substantially flatter than that derived from the WSO photospheric map for CR 1913 (Fig. 11, right) or from the C2 observations themselves (Fig. 5). We conclude that the observed increase in the latitudinal extent of the streamer belt between CR 1911 and CR 1913 was caused mainly by new flux eruptions rather than by surface transport effects.

Using simulations (not displayed here) in which the observed active regions were represented by equivalent magnetic doublets, we confirmed that it was the large, southern-hemisphere active region centered around longitude 255°, and not the smaller, new-cycle region located to its northwest near latitude 23° north, which was mainly responsible for warping the current sheet from CR 1911 onward. In these simulations, the effect of each active region on the streamer belt configuration was determined by depositing the equivalent doublet source onto a numerical grid representing the photospheric field before the active region erupted.

Finally, it is interesting to consider how the streamer belt would evolve if no activity occurred over an extended period of time. To investigate this question, we initialize the flux transport calculation with the WSO map for CR 1913 and evolve the photospheric field for 13 rotations without depositing any new flux (see Fig. 12). As the non-axisymmetric field component decays, the streamer belt gradually flattens toward the equator. The decay timescale is effectively determined by the 10 m s^{-1} meridional flow, which carries the remnant active-region flux to middle latitudes, where it is rapidly sheared by differential rotation and annihilated by diffusion (for a more detailed description of these process, see § 3.3 in Wang & Sheeley 1991). The streamer belt thus becomes flat after about one year. In reality, however, the nonaxisymmetric field component is likely to be continually regenerated by new activity.

6. CONCLUSIONS

Our simulations suggest that the large-scale streamer structure observed by LASCO during 1996 can be represented by a single, tilted and warped current sheet encircling the Sun. The spikelike features appearing in the individual C2 and C3 images correspond to locations where the current sheet is viewed edge-on; depending on the shape of the current sheet, single, double, or multiple structures may be seen at either limb. The presence of even narrower spikes and rays in the LASCO images may indicate that the scattering layer is lumpy or filamentary on small scales, as well as warped on large scales. Somewhat analogous fine structure is produced by the finite grid resolution of the simulations (see also Wang 1996).

The observed changes in the streamer belt structure between 1996 June and 1996 September were caused by flux emergence within a low-latitude active region complex. However, our simulations have shown that the effect of photospheric activity on the topology of the current sheet and streamer belt depends not just on the strength of the erupting flux, but also on its longitudinal phase relative to the background field. Thus the initial appearance of a strong bipolar magnetic region during CR 1909 did not lead to a widening of the streamer belt because the low-order multipoles of the new active region were almost 180° out of phase with the original background field. The streamer belt only began to widen two rotations later, when the equato-
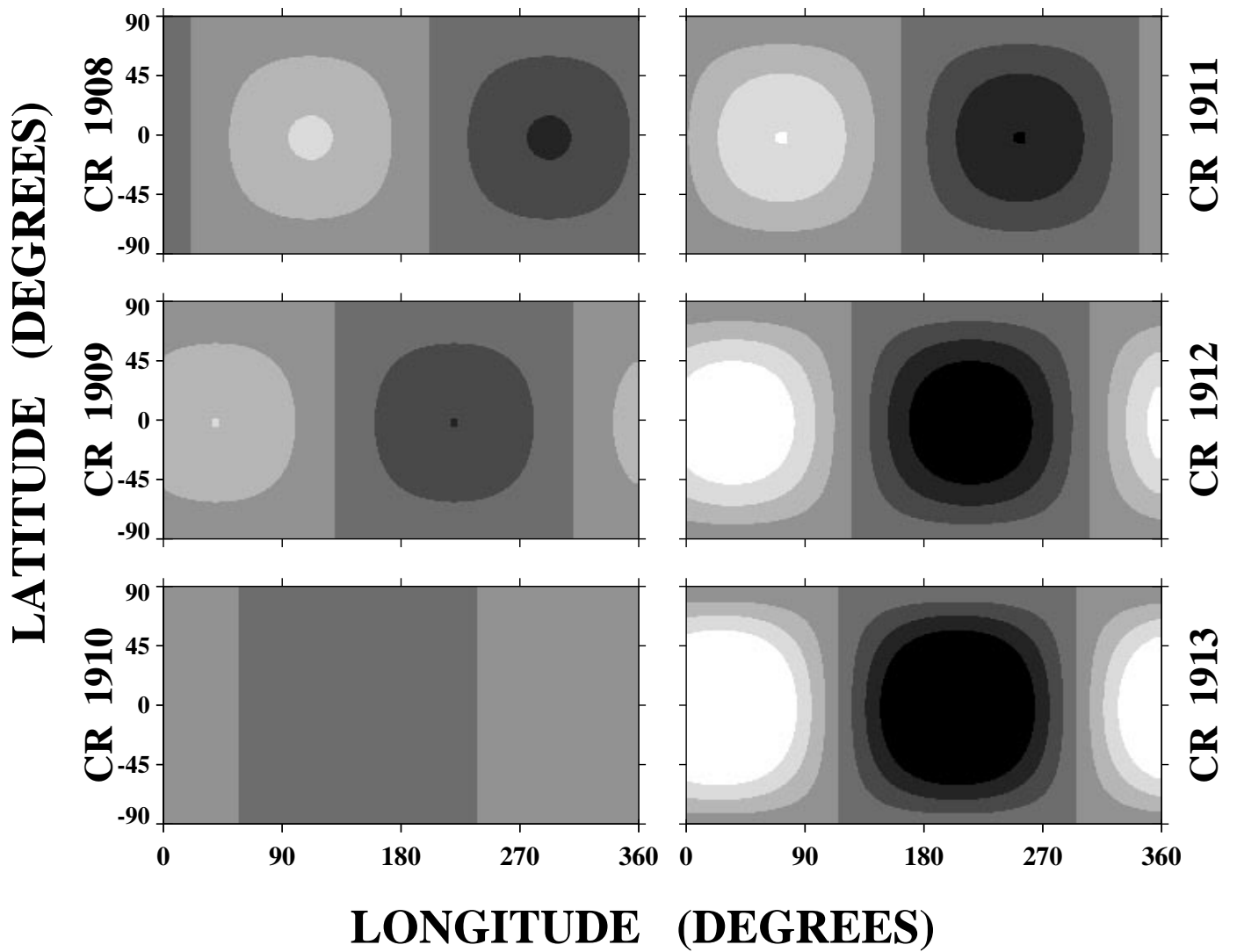
FIG. 9.—Equatorial dipole field b_{11} at $r = 2.5\ R_\odot$, derived from the WSO photospheric field maps for CR 1908–1913 (Fig. 6). Black denotes $b_{11} < -0.04$ G, white denotes $b_{11} > 0.04$ G, while intermediate shades indicate fields in the range $-0.04\ \text{G} < b_{11} < 0.04\ \text{G}$.
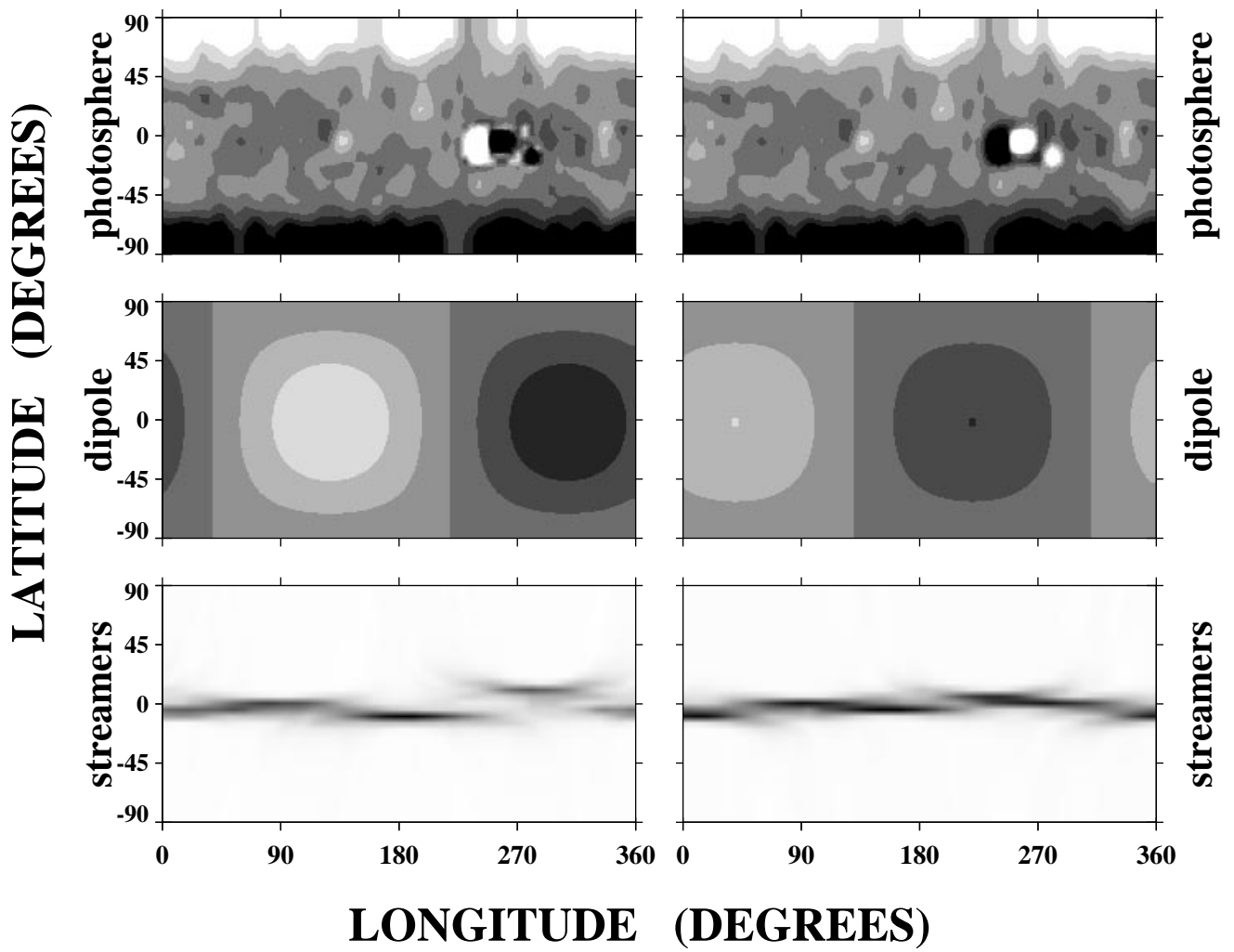
FIG. 10.—Effect of reversing the east-west polarity of the active region complex in CR 1909 (*left*). Because the equatorial dipole components of the bipoles and the background field are now in phase with each other, the streamer belt shows a greater latitudinal excursion than in the original case (*right*).
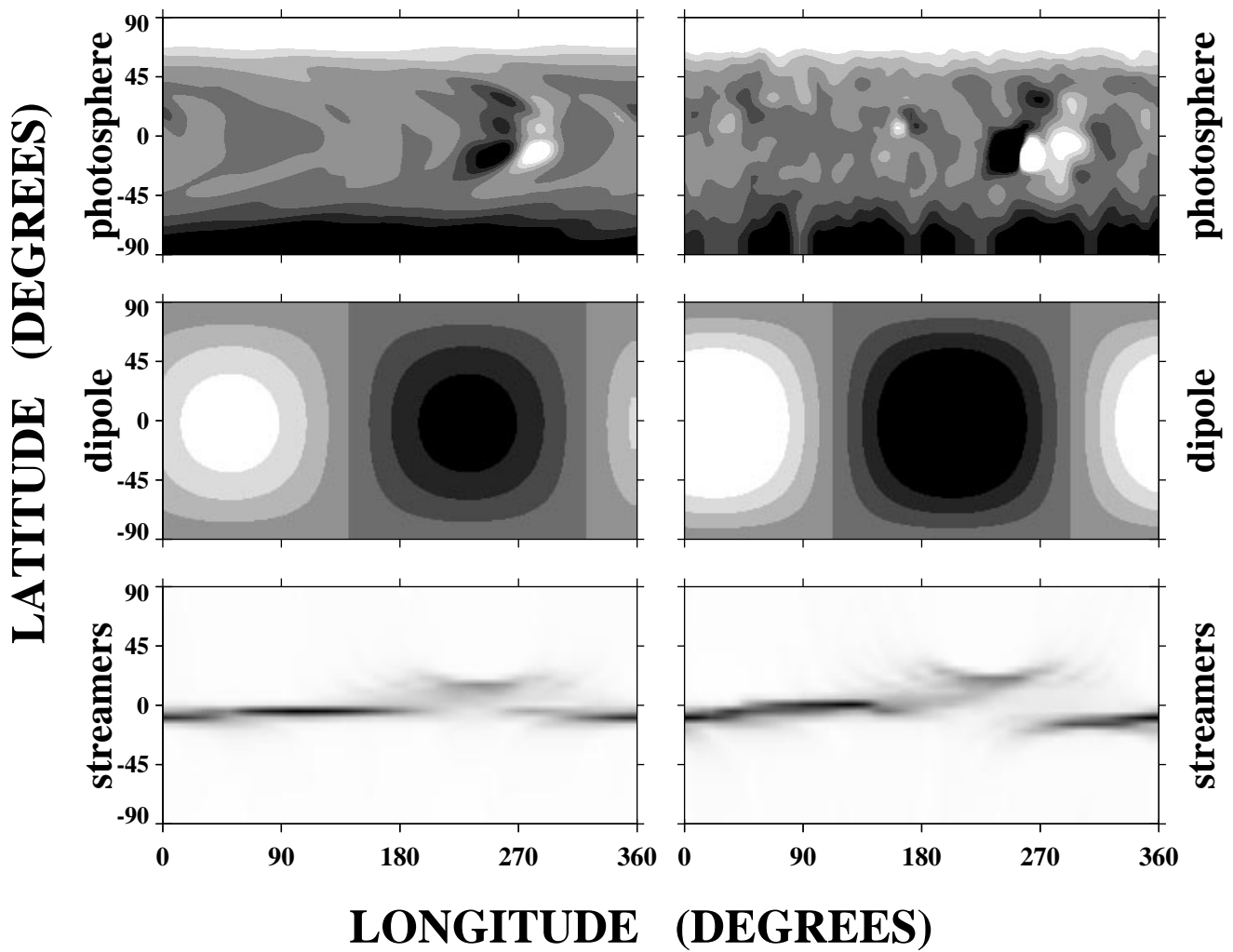
FIG. 11.—Left panels illustrate how the photospheric field, equatorial dipole, and streamer structure would have appeared during CR 1913 if no new flux had erupted over the previous two rotations. The WSO photospheric field map for CR 1911 was evolved in time including only transport effects (differential rotation, supergranular diffusion, and meridional flow). Right panels show the corresponding maps based on the observed photospheric field for CR 1913.
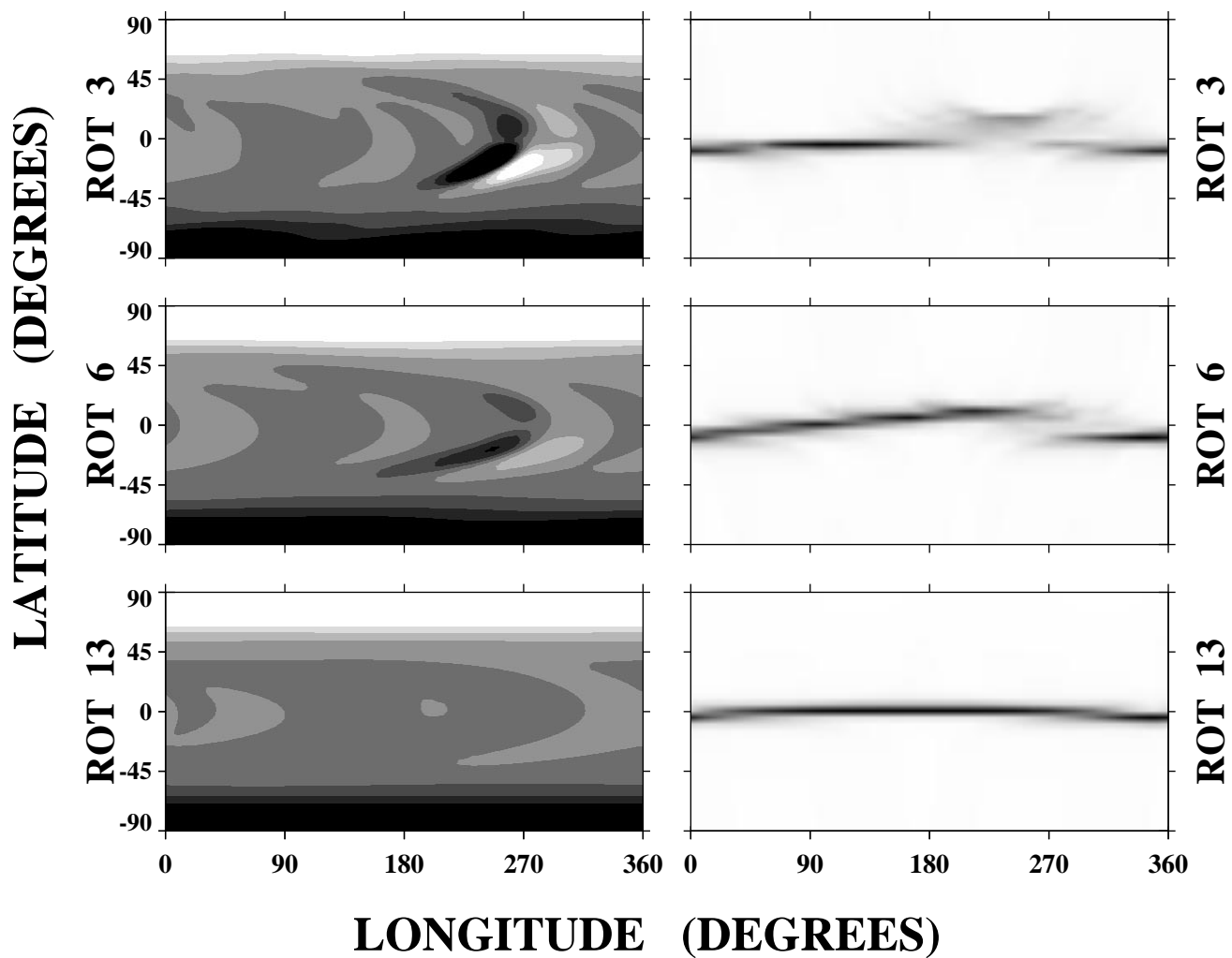
FIG. 12.—Simulation illustrating the decay of the active region flux and the flattening of the streamer belt in the hypothetical absence of any new activity after 1996 September. The observed photospheric field for CR 1913 was evolved for 13 rotations including only transport effects.

rial dipole was regenerated by new activity within the same large complex.

REFERENCES

Billings, D. E. 1966, A Guide to the Solar Corona (New York: Academic)
Brueckner, G. E., et al. 1995, Sol. Phys., 162, 357
Bruno, R., Burlaga, L. F., & Hundhausen, A. J. 1982, J. Geophys. Res., 87, 10339
DeVore, C. R., Sheeley, N. R., Jr., & Boris, J. P. 1984, Sol. Phys., 92, 1
Hoeksema, J. T. 1984, Ph.D. thesis, Stanford Univ.
Howard, R. A., & Koomen, M. J. 1974, Sol. Phys., 37, 469
Howard, R. A., Sheeley, N. R., Jr., Koomen, M. J., & Michels, D. J. 1985, J. Geophys. Res., 90, 8173
Pneuman, G. W., Hansen, S. F., & Hansen, R. T. 1978, Sol. Phys., 59, 313
Schatten, K. H. 1971, Cosmic Electrodyn., 2, 232
Schatten, K. H., Wilcox, J. M., & Ness, N. F. 1969, Sol. Phys., 6, 442
Svalgaard, L., Duvall, T. L., Jr., & Scherrer, P. H. 1978, Sol. Phys., 58, 225
Ulrich, R. K. 1992, in Cool Stars, Stellar Systems, and the Sun, ed. M. S. Giampapa & J. A. Bookbinder (San Francisco: ASP), 265
Wang, Y.-M. 1996, ApJ, 456, L119
Wang, Y.-M., & Sheeley, N. R., Jr. 1991, ApJ, 375, 761
———. 1992, ApJ, 392, 310
———. 1993, ApJ, 414, 916
———. 1995, ApJ, 447, L143
Wang, Y.-M., Nash, A. G., & Sheeley, N. R., Jr. 1989, ApJ, 347, 529